▌ Perovskites

Local A-Site Layering in Rare-Earth Orthochromite Perovskites by Solution Synthesis

Luke M. Daniels,[a] Reza J. Kashtiban,[b] Demie Kepaptsoglou,[c] Quentin M. Ramasse,[c] Jeremy Sloan,[b] and Richard I. Walton*[a]

Abstract: Cation size effects were examined in the mixed A-site perovskites $La_{0.5}Sm_{0.5}CrO_3$ and $La_{0.5}Tb_{0.5}CrO_3$ prepared through both hydrothermal and solid-state methods. Atomically resolved electron energy loss spectroscopy (EELS) in the transmission electron microscope shows that while the La and Sm cations are randomly distributed, increased cation-radius variance in $La_{0.5}Tb_{0.5}CrO_3$ results in regions of localised La and Tb layers, an atomic arrangement exclusive to the hydrothermally prepared material. Solid-state preparation gives lower homogeneity resulting in separate nanoscale regions rich in La^{3+} and Tb^{3+}. The A-site layering in hydrothermal $La_{0.5}Tb_{0.5}CrO_3$ is randomised upon annealing at high temperature, resulting in magnetic behaviour that is dependent on synthesis route.

Perovskites ABX_3 are one of the most versatile group of materials in solid-state chemistry with respect to valence and ionic radii of the possible incorporated cations A and B, as well choice of anion X, from oxide to halides. This compositional and structural flexibility allows a variety of distortions from the archetypical cubic perovskite structure mediated through phenomena such as cation displacements, octahedral tilts, ordered vacancies and Jahn–Teller effects. For perovskite oxides, this gives rise to interesting and functional properties, such as high-temperature superconductivity, piezoelectricity and ferroelectricity, colossal magnetoresistance, multiferroism and catalytic activity.[1]

More subtle cation order/disorder effects can result when multiple metals share the same crystallographic position;[2] in particular, ordered cation arrangements are probable when their charge and/or ionic radii differ sufficiently.[3] Ordered arrangements of mixed B site cations are observed more frequently than those of the A site.[4] Rock-salt ordering of B sites in compositions $A_2BB'X_6$ is commonplace, while layered configurations of the A sites in compositions $AA'B_2X_6$ or $AA'BB'X_6$ are found when they provide lower bonding strains with the neighbouring anions.[5] For those materials, layered A site arrangements result from effects driven by the B site ordering, such as anion vacancies, A site vacancies and second-order Jahn–Teller distortions.[6] A review of the literature shows that it is rare for stoichiometric perovskites to exhibit long-range A site order in the absence of an ordered B/B' sublattice, with layering effects being observed only on the local scale without B site ordering in materials such as $NaLa(BB')O_6$ (B = Fe or Mn, and B' = Nb or Ta), in which B site second-order Jahn–Teller effects and charge difference between the Na^+ and La^{3+} are the driving mechanisms.[7] Structural order may be driven by anion vacancies, such as the ordered cation arrangements of the triple perovskites, $YBa_2Cu_3O_{7-x}$ and $YBa_2Fe_3O_{8+x}$, with separate eight- and ten-coordinate A sites, respectively.[8] In this paper we investigate the possibility of A site order in chromite perovskites, in which by using a single B site cation and isovalent lanthanides on the A site we negate the common mechanisms for A site order. In doing so, we are able to observe the direct effects of cation radius variance on A site ordering in mixed rare-earth orthochromite perovskites.

Rare-earth orthochromite perovskites are already known to exhibit a plethora of properties,[9] and it is their magnetoelectric properties that have produced most interest, firstly with the theoretical prediction of a spontaneous electrical polarisation,[10] followed by the experimental observation of both canted antiferromagnetism and polarisation in several $RCrO_3$ oxides (R = Sm^{3+}, Gd^{3+}, Tb^{3+}, Er^{3+} and Tm^{3+}),[11] and observations of spin–phonon couplings as a result of magnetically induced symmetry breaking.[12] Recently, it was shown that the presence of a magnetic R^{3+} cation is not necessary to generate such behaviour,[13] and current theoretical work suggests that these polarisations can be tuned by external magnetic fields.[14] We have previously shown how hydrothermal conditions at approximately 400 °C can be used to form well-crystallised samples of rare-earth orthochromites with magnetic properties that match those from conventional synthesis.[15] Herein, we compare synthesis routes of new mixed A site examples, not previously reported by any synthetic method, in which extreme A-site radius variance leads to preparation-dependent local structure and, in turn, magnetic properties.

[a] Dr. L. M. Daniels, Prof. R. I. Walton
Department of Chemistry, University of Warwick, Coventry, CV4 7AL (UK)
E-mail: r.i.walton@warwick.ac.uk

[b] Dr. R. J. Kashtiban, Dr. J. Sloan
Department of Physics, University of Warwick, Coventry, CV4 7AL (UK)

[c] Dr. D. Kepaptsoglou, Prof. Q. M. Ramasse
SuperSTEM Laboratory, SciTech Daresbury Campus
Daresbury, WA4 4AD (UK)

Crystalline $La_{0.5}Sm_{0.5}CrO_3$ and $La_{0.5}Tb_{0.5}CrO_3$ were each produced through two distinct synthetic routes involving very different reaction temperatures; the hydrothermal treatment of an amorphous mixed-metal hydroxide at approximately 400 °C,[15a] and conventional solid-state synthesis, in which the same amorphous mixed-metal precursors were fired at temperatures of 1200 °C or higher in air. Hydrothermal synthesis produced phase-pure powders of $La_{0.5}Sm_{0.5}CrO_3$ and $La_{0.5}Tb_{0.5}CrO_3$ at temperatures of 375 °C (for 6 h) and 410 °C (for 12 h), respectively, whilst solid-state reactions were performed at 1200 °C (for 12 h) and 1400 °C (for 96 h).

The resulting product of each reaction (Figure 1 a, b and the Supporting Information, Figure S1) is phase pure by powder X-ray diffraction (PXRD). The patterns of all four materials were indexed to the orthorhombic space group *Pnma*, and Rietveld analysis showed their structures to be that of the classical $GdFeO_3$ distorted perovskite. No evidence for ordering effects of separate lanthanide sites was observed in the powder diffraction data (such as a contracted unit cell that might result from segregation of A sites into layers), and both the La^{3+} and

Sm^{3+}, and the La^{3+} and Tb^{3+}, were modelled on the same crystallographic 4c position $(x, \frac{1}{4}, z)$ with split occupancy. The refined lattice parameters of both materials display a linear dependence between the respective single lanthanide end members, following Vegard's law (the Supporting Information, Table S1 and Figure S2). The smaller mean ionic radius of the A site in $La_{0.5}Tb_{0.5}CrO_3$ results in increased tilting of the CrO_6 octahedra, compared to $La_{0.5}Sm_{0.5}CrO_3$, giving a smaller unit cell volume.

The lattice parameters of the materials produced through the two synthesis routes agree within 0.2 % for $La_{0.5}Sm_{0.5}CrO_3$ and 0.4 % for $La_{0.5}Tb_{0.5}CrO_3$ (the Supporting Information, Table S2). PXRD suggests that the hydrothermally prepared materials are the more crystalline powders, as broader peaks were observed for the solid-state samples. In addition, transmission electron microscopy (TEM) shows that hydrothermal treatment of the amorphous precursors leads to increased homogeneity of particle morphology and size compared to those fired at 1200 °C or above. Dendritic morphologies of a few μm in size are observed for both hydrothermal samples (Figure 1 c, e), whereas a much greater distribution of particle size is observed for the solid-state prepared materials, ranging from 0.1 up to 10 μm (Figure 1 d, f).

Raman spectra (the Supporting Information, Figure S3) display mode-softening behaviour towards $LaCrO_3$, as was observed in all $RCrO_3$,[15c] and the increased breadth of the observed bands in $La_{0.5}Tb_{0.5}CrO_3$ gave an indication of compositional disorder present on the A site. Compositional disorder in $A_xA'_{1-x}BX_3$ materials can be quantified by the statistical variance (σ^2) of the ionic radii of the two A-site cations present, with higher variance referring to greater size disparity. The importance of this was emphasised by Attfield, who showed cation-radius variance to affect the magnetoresistive properties of doped lanthanide manganite materials ($La_{1-x}Sr_xMnO_3$) and cuprate superconductors ($La_{2-x}Sr_xCuO_4$).[16] To the best of our knowledge, the new $La_{0.5}Tb_{0.5}CrO_3$ composition has the largest A-site radius variance of any mixed rare-earth chromite reported to date, 25 % greater than that of $La_{0.5}Gd_{0.5}CrO_3$,[17] (Figure 2 a, b). It is possible that the longer synthesis durations and higher temperatures required for $La_{0.5}Tb_{0.5}CrO_3$ by both synthetic routes (the Supporting Information, Figure S4) are associated with this increased radius variance compared to those of $La_{0.5}Sm_{0.5}CrO_3$. Using the lower temperature and shorter reaction time needed for $La_{0.5}Sm_{0.5}CrO_3$ resulted in the presence of hydroxide impurities in the hydrothermal $La_{0.5}Tb_{0.5}CrO_3$ material. Attempts were made to produce solid solutions with greater variance, such as $La_{0.5}Ho_{0.5}CrO_3$ and $La_{0.5}Yb_{0.5}CrO_3$ (the Supporting information, Figure S5); however, these did not result in single phases, suggesting the existence of a synthetic A-site radius variance limit.

High-angle annular dark field scanning transmission electron microscopy (HAADF-STEM) and electron energy loss spectroscopy (EELS) were performed on crystallites aligned along the [101] zone axis in the *Pnma* setting (equivalent to pseudo cubic [100] projection of $Pm\bar{3}m$), which provided large separation between neighbouring A and B site columns, ideal for EELS mapping. The lanthanides appeared as brighter columns
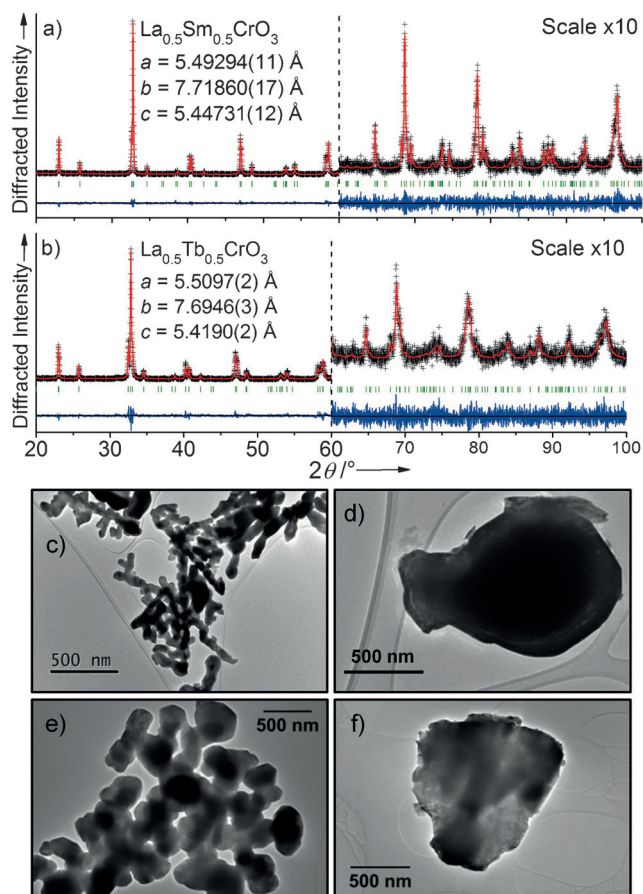

Figure 1. Rietveld refinements performed against room temperature PXRD data ($\lambda = 1.54056$ Å) of hydrothermal samples of a) $La_{0.5}Sm_{0.5}CrO_3$ and b) $La_{0.5}Tb_{0.5}CrO_3$. The regions $60 \leq 2\theta \leq 100$ are scaled to display the fits at higher angle. Observed data (black crosses), calculated (red line), and difference (blue line) patterns are shown. Green tick marks denote positions of expected reflections for space group *Pnma*. TEM images compare particle morphologies between hydrothermal and solid-state-prepared materials of c),d) $La_{0.5}Sm_{0.5}CrO_3$ and e),f) $La_{0.5}Tb_{0.5}CrO_3$, respectively.

In figure panel a): $La_{0.5}Sm_{0.5}CrO_3$, $a = 5.49294(11)$ Å, $b = 7.71860(17)$ Å, $c = 5.44731(12)$ Å, Scale x10.

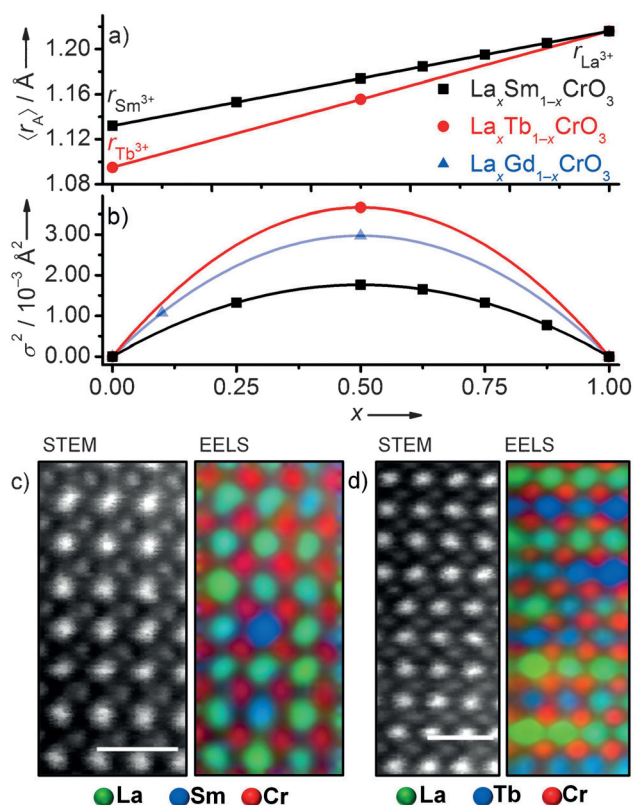In figure panel b): $La_{0.5}Tb_{0.5}CrO_3$, $a = 5.5097(2)$ Å, $b = 7.6946(3)$ Å, $c = 5.4190(2)$ Å, Scale x10.

Figure 2. Variation in mean rare-earth A-site cation: a) radii and b) variance for $La_xSm_{1-x}CrO_3$ (black), $La_xTb_{1-x}CrO_3$ (red) solid solutions. Variance of $La_xGd_{1-x}CrO_3$ reported previously is included for comparison (blue).[17] Points along each line represent solid solutions synthesised in the present and previous studies.[15a] HAADF-STEM images and corresponding EELS maps of hydrothermal c) $La_{0.5}Sm_{0.5}CrO_3$ and d) $La_{0.5}Tb_{0.5}CrO_3$ crystallites aligned along the [101] zone axis. Scale bars represent 1 nm.

to the larger La^{3+} and smaller Tb^{3+}; the segregation of the two different sized lanthanides into layers likely reduces this strain within the local structure. The observation of such layering suggests that the structural distortion, typically mediated through octahedral tilting in perovskites, is inhomogeneous. The short scales on which these inhomogeneities exist are below the observable limit of other techniques, such as PXRD and Raman scattering, both of which present no evidence for long range lattice ordering of the A-site cations, and so a tilt system cannot be assigned.
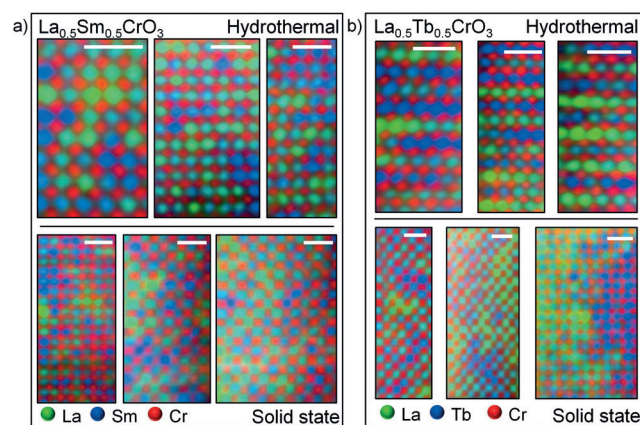

Figure 3. Comparison of EELS maps recorded along the [101] direction of hydrothermal (upper) and solid state (lower) materials in a) $La_{0.5}Sm_{0.5}CrO_3$ and b) $La_{0.5}Tb_{0.5}CrO_3$. The white scale bars in each image represent 1 nm.

in the HAADF images (the Supporting Information, Figure S6), and distinguishing between the two rare-earths in each material is difficult due to their similar values of Z ($Z_{La} = 57$, $Z_{Sm} = 62$ and $Z_{Tb} = 65$). Although direct observations of local A-site cation ordering have previously been made by using HAADF-STEM,[7] and local cation chemistry of complex perovskites can in some cases be determined by imaging alone,[18] the contrast between the lanthanides used in the current study requires the use of EELS for the pairs to be distinguished in practice. The EELS maps (Figure 2c, d) showed atomic-scale differences in lanthanide distribution between hydrothermal $La_{0.5}Sm_{0.5}CrO_3$ and $La_{0.5}Tb_{0.5}CrO_3$. Localised layered-like ordering of the A-site cations was observed in the $La_{0.5}Tb_{0.5}CrO_3$ sample, Figure 2d, compared to random distributions present in $La_{0.5}Sm_{0.5}CrO_3$ (Figure 2c). EELS spectra were collected from numerous crystallites in each sample to ensure that these observations represented the bulk sample (the Supporting Information, Figure S7, S8, S9 and S10). The only plausible explanation for these observations is the increased A-site radius variance of the $La_{0.5}Tb_{0.5}CrO_3$ composition, because there is no possible influence from vacancy ordering, charge, or Jahn–Teller effects, as has been seen in other known A-site ordered perovskites. The formation of these La and Tb layers must only result from the size-induced strain that exists between each environment local

The two methods used to synthesise these solid solutions also lead to different atomic-scale variations in lanthanide distribution (Figure 3). For $La_{0.5}Sm_{0.5}CrO_3$, the EELS maps of samples prepared by hydrothermal and solid-state methods showed a similar, random, lanthanide distribution. However, unlike the relatively homogeneous distributions of $La_{0.5}Sm_{0.5}CrO_3$, the two $La_{0.5}Tb_{0.5}CrO_3$ materials are significantly different from each other, with no evidence of the layered-like hydrothermal arrangements being present in the solid-state material. Instead in the solid-state sample of $La_{0.5}Tb_{0.5}CrO_3$, large domains of La-rich and Tb-rich regions, several nanometres in size, were observed, large enough to be observed through careful analysis of the STEM images (the Supporting Information, Figure S11), which showed separate regions of $LaCrO_3$ and $TbCrO_3$, with different degrees of cation displacement. This suggests the formation of the locally layered hydrothermal material represents a metastable phase. This was supported by differential scanning calorimetry (DSC), which showed a thermal event exclusive to hydrothermal $La_{0.5}Tb_{0.5}CrO_3$ at 1200 °C compared to the solid-state and annealed as-made materials (the Supporting Information, Figure S12). This is indicative that the layered cation configurations of hydrothermal $La_{0.5}Tb_{0.5}CrO_3$ are randomised upon annealing to high temperature with the local A-site ordering being diminished. The hydrothermal synthesis route is already known to produce metastable layered perovskite phases, such as $LaBaMn_2O_6$, with ceramic synthesis leading to the disor-

dered La$_{0.5}$Ba$_{0.5}$MnO$_3$,[19] but in that case, the A-site cations have different charges and the B-site is mixed valent. Indeed, in other mixed lanthanide–barium manganites, the choice of synthesis routes may result in either ordered or disordered A site distributions.[20] Previously, thermal destabilisation of A site cationic order at 1100 K has been reported in YBaMn$_2$O$_6$,[21] resulting in the random A-site distributions of Y$_{0.5}$Ba$_{0.5}$MnO$_3$.

The local ordering of A-site metals manifests itself in bulk magnetic properties. We note that the temperature dependence of the magnetic susceptibility of hydrothermal La$_{0.5}$Tb$_{0.5}$CrO$_3$ (the Supporting Information, Figure S13) is indicative of a homogeneous solid solution, exhibiting a linear trend in T_N (arising from ordering of Cr^{3+} spins above 200 K) between the end members. The decrease in T_N towards TbCrO$_3$ highlights the increased distortion of the structure and is greatly dependent on virtual charge transfer between the Cr^{3+} t$_{2g}$ and e$_g$ orbitals, which are hybridised as a result of π and σ bond overlap.[22] The small ferromagnetic component induced by the canted Cr^{3+} AFM sublattice produced a polarisation of the paramagnetic Tb^{3+} spins, which decouple only at low temperatures to order in an AFM fashion.[23] This is represented by the observed downturn in the data at low temperatures.
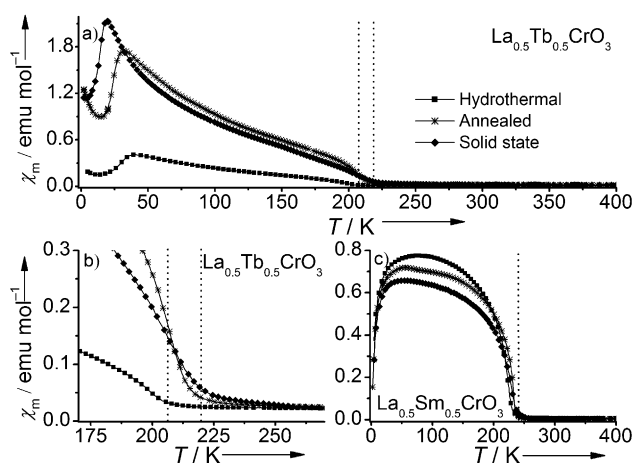

Figure 4. Temperature dependence of molar magnetic susceptibility data (FCC) for a) La$_{0.5}$Tb$_{0.5}$CrO$_3$ prepared through hydrothermal (black line), annealed (red line) and solid-state (blue line) synthetic methods in an applied field of 100 Oe. An enlarged plot of the T_N region is shown in b), while c) shows the same FCC data for La$_{0.5}$Sm$_{0.5}$CrO$_3$. The red dotted lines indicate ordering of the Cr^{3+} spins at T_N.

Clear differences were observed in the susceptibility data of La$_{0.5}$Tb$_{0.5}$CrO$_3$ produced through hydrothermal and solid-state techniques (Figure 4a), which must be a consequence of the atomic-scale lanthanide distributions described above. The lower T_N observed for hydrothermal La$_{0.5}$Tb$_{0.5}$CrO$_3$ compared to the solid-state and annealed materials (Figure 4b) must result from the localised A-site ordering, with the more distorted Tb^{3+}-rich layers disrupting the superexchange interactions between adjacent Cr^{3+} spins. In contrast, minor differences were observed between the magnetic susceptibility data of La$_{0.5}$Sm$_{0.5}$CrO$_3$ materials prepared by different methods (Fig-

ure 4c), with all samples displaying similar low-temperature behaviour, and which is consistent with previously obtained data from the same composition, in which spin reorientation of chromium gave a broad ordering feature.[15a]

In La$_{0.5}$Tb$_{0.5}$CrO$_3$, further differences in magnetic behaviour between the hydrothermal and solid-state materials arise at low temperatures, when the hydrothermal sample exhibited a higher Tb^{3+} ordering temperature (ca. 25 K) and much lower susceptibility. We propose that the exchange pathways for Tb-
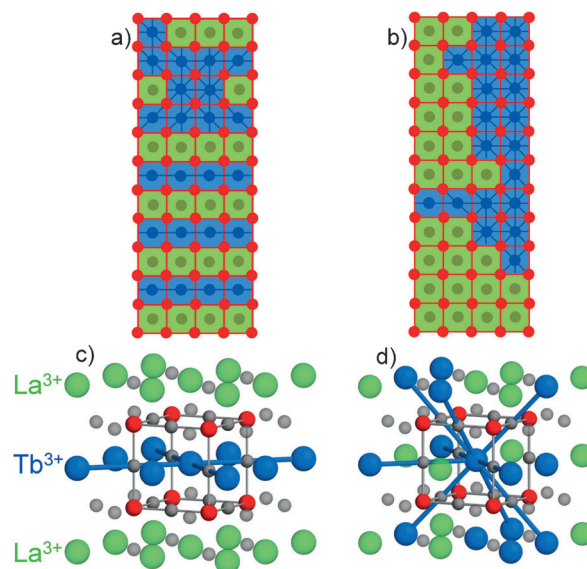

Figure 5. Schematic structural diagrams of La$_{0.5}$Tb$_{0.5}$CrO$_3$ perovskite viewed along the [101] direction showing how lanthanide distributions influence the formation of magnetic superexchange pathways between neighbouring Tb^{3+} cations. Distributions a) and b) are constructed from actual EELS maps shown in Figure 3b. Each square represents a single ABO_3 unit, the colour detailing the lanthanide present at its centre (green La^{3+}, blue Tb^{3+}). The B-site lattice is shown in red and red lines show AFM superexchange pathways between neighbouring Cr^{3+} ions, which are affected only by structural distortion. Blue lines represent magnetic-exchange pathways between Tb^{3+} cations, in which they can form. The environments local to a Tb^{3+} cation are shown in c) the layered hydrothermal structure, and d) with random lanthanide distribution. Atom colours: La green, Tb blue, Cr red, and O grey. Tb-O-Tb superexchange pathways are shown as blue lines.

O-Tb interactions form across the edge-to-edge diagonal of the primitive ABO_3 cell, giving rise to two-dimensional interactions occurring within the layered arrangement, and are not able to form a 3D network (Figure 5a). Interactions between each Tb^{3+} layer are inhibited by the intercalating layers of non-magnetic La^{3+} (Figure 5c). For the solid-state material, the reduced Tb^{3+} ordering temperature and increased susceptibility observed below T_N resulted from the 3D exchange pathways that can form within the nanoscale regions of TbCrO$_3$ (Figure 5b), which dominate the susceptibility of La$_{0.5}$Tb$_{0.5}$CrO$_3$ at low temperature.

Changes in the magnetic susceptibility were observed when annealing the as-made hydrothermal La$_{0.5}$Tb$_{0.5}$CrO$_3$ to 1400 °C, supporting the DSC measurements that indicated a randomisation of the layered hydrothermal configuration. Annealing to 1400 °C showed a maximum susceptibility comparable to

solid-state $La_{0.5}Tb_{0.5}CrO_3$ but a low-temperature line shape similar to that of the hydrothermal method. The DSC data suggested that randomisation occurred at $1000\,°C$, but required the high temperature of $1400\,°C$ to achieve completion. The more randomised distribution of lanthanides would allow increased super-exchange interactions compared to the layered arrangement (Figure 5d), giving rise to a much larger magnetic response below T_N.

In conclusion, we have presented evidence of local A-site layering in a perovskite structure induced exclusively by A-site cation size variance. This order is then removed by high-temperature annealing, giving randomised distributions of the A-site substituents. The locally ordered A site cation distribution in hydrothermal $La_{0.5}Tb_{0.5}CrO_3$ arises only from the size difference between the A-site metals: their radius variance appears to be at the limit of what is synthetically possible, as was evidenced by the solid-state sample, which shows significant nanoscale separation of the lanthanides. Other literature examples of A-site ordering in perovskites are associated with B-site ordering, and/or charge difference between A -site metals, or oxide vacancies. Locally ordered hydrothermal $La_{0.5}Tb_{0.5}CrO_3$ is thus a unique metastable phase with distinct low-temperature magnetic behaviour, inaccessible through conventional ceramic synthesis. Assuming the metals are homogeneously distributed in solution during synthesis, we speculate that this gives the structure the kinetic possibility of ordering at the point of crystal growth, something not possible by solid-state reactions, which are limited by the much slower diffusion of ions in the solid state.

Experimental Section

The synthesis of $La_xSm_{1-x}CrO_3$ ($x = 0.5$) was performed by using the high-temperature hydrothermal treatment of an amorphous mixed-metal hydroxide precursor detailed previously.[15a] The $La_xTb_{1-x}CrO_3$ ($x = 0.5$) amorphous precursor was produced by the same method; however, pure samples of the perovskite were formed only after 12 h of hydrothermal treatment at $410\,°C$, under $200+$ bar of autogeneous pressure, compared to the shorter 6 h reactions at $375\,°C$ for $La_{0.5}Sm_{0.5}CrO_3$. For the conventional solid-state syntheses, the same amorphous precursors were used for these reactions. The powdered precursors were placed in alumina crucibles and fired at $1200\,°C$ for 12 h for $La_{0.5}Sm_{0.5}CrO_3$, whereas the synthesis of $La_{0.5}Tb_{0.5}CrO_3$ involved a total of four 24 h firing cycles to $1400\,°C$, with regrinding of the powder in between each cycle (the Supporting Information, Figure S14).

High-resolution powder X-ray diffraction (PXRD) data were collected by using a Panalytical X'Pert Pro MPD (Cu$_{K\alpha1}$, $\lambda = 1.54056$ Å). Rietveld refinements against the data were performed by using TOPAS-Academic implemented with jEdit (Versions 4.1 and 4.3.1, respectively).[24] The magnetic properties of the solid solutions were investigated by using a quantum design magnetic property measurement system (MPMS) SQUID magnetometer. The field-cooled cooling (FCC) data were collected in an applied magnetic field of 100 Oe. For STEM imaging and EELS, polycrystalline samples were ultrasonically dispersed in a methanol suspension onto lacy carbon film reinforced by a copper grid. TEM images were acquired using a JEOL 2100 instrument equipped with a LaB$_6$ filament operating at 200 kV, while HRTEM images were acquired

using a third-order (C_3) aberration corrected JEOL ARM200F operating at a voltage of 200 kV. High-angle annular dark field (HAADF) scanning transmission electron microscopy (STEM) imaging was performed by using a Nion Ultrastem 100 microscope with cold-field emission gun operating at 100 kV, equipped with a Gatan Enfina spectrometer at the SuperSTEM facility in Daresbury, U.K. The probe-forming optics were configured to form an approximately 0.9 Å probe (full width at half-maximum) with a convergence angle of 30 mrad and a probe current of 100 pA. The native energy spread of the electron probe was 0.35 eV, and the collection semi-angle for the EELS measurements was 36 mrad. Chemical maps were produced by rastering the electron probe serially across a defined region and collecting an EEL spectrum at each point. Chemical maps were created by integrating at each point of these spectrum images the spectrum intensity over an approximately 60 eV window above the Cr L$_{2,3}$, La M$_{4,5}$, Tb M$_{4,5}$ and Sm M$_{4,5}$ EELS edge onsets after background subtraction by using a linear combination of power laws using the ImageJ image processing software implemented with the Cornell spectrum imaging (CSI) plugin.[25] The individual EELS maps for Cr, La, Sm and Tb were denoised through smoothing in ImageJ before combining into single RGB plots.

[1] a) A. S. Bhalla, R. Guo, R. Roy, *Mater. Res. Innovations* **2000**, *4*, 3–26; b) M. A. Peña, J. L. G. Fierro, *Chem. Rev.* **2001**, *101*, 1981–2017.
[2] P. K. Davies, *Curr. Opin. Solid State Mater. Sci.* **1999**, *4*, 467–471.
[3] F. Galasso, W. Darby, *J. Phys. Chem.* **1962**, *66*, 131–132.
[4] M. C. Knapp, P. M. Woodward, *J. Solid State Chem.* **2006**, *179*, 1076–1085.
[5] G. King, P. M. Woodward, *J. Mater. Chem.* **2010**, *20*, 5785–5796.
[6] G. King, S. Thimmaiah, A. Dwivedi, P. M. Woodward, *Chem. Mater.* **2007**, *19*, 6451–6458.
[7] W. Dachraoui, T. Yang, C. Liu, G. King, J. Hadermann, G. Van Tendeloo, A. Llobet, M. Greenblatt, *Chem. Mater.* **2011**, *23*, 2398–2406.
[8] a) C. Chaillout, M. A. Alario-Franco, J. J. Capponi, J. Chenavas, J. L. Hodeau, M. Marezio, *Phys. Rev. B* **1987**, *36*, 7118–7120; b) P. Karen, A. Kjekshus, Q. Huang, V. L. Karen, J. W. Lynn, N. Rosov, I. Natali Sora, A. Santoro, *J. Solid State Chem.* **2003**, *174*, 87–95.
[9] a) J. Beckers, G. Rothenberg, *ChemPhysChem* **2005**, *6*, 223–225; b) N. Russo, D. Mescia, D. Fino, G. Saracco, V. Specchia, *Ind. Eng. Chem. Res.* **2007**, *46*, 4226–4231; c) J. Fergus, *Solid State Ionics* **2004**, *171*, 1–15; d) Z. Liu, D. Dong, X. Huang, Z. Lu, Y. Sui, X. Wang, J. Miao, Z. X. Shen, W. Su, *Electrochem. Solid-State Lett.* **2005**, *8*, A250–A252; e) Y. Shen, M.

Liu, T. He, S. P. Jiang, *J. Power Sources* **2010**, *195*, 977–983; f) M. Siemons, U. Simon, *Sens. Actuators B* **2007**, *126*, 181–186.

[10] A. K. Zvezdin, A. A. Mukhin, *JETP Lett.* **2008**, *88*, 505–510.

[11] a) B. Rajeswaran, D. I. Khomskii, A. K. Zvezdin, C. N. R. Rao, A. Sundaresan, *Phys. Rev. B* **2012**, *86*, 214409–214414; b) J. R. Sahu, C. R. Serrao, N. Ray, U. V. Waghmare, C. N. R. Rao, *J. Mater. Chem.* **2007**, *17*, 42–44.

[12] a) V. Srinu Bhadram, B. Rajeswaran, A. Sundaresan, C. Narayana, *EPL* **2013**, *101*, 17008–17014; b) M. El Amrani, M. Zaghrioui, V. Ta Phuoc, F. Gervais, N. E. Massa, *J. Magn. Magn. Mater.* **2014**, *361*, 1–6.

[13] a) K. R. S. P. Meher, C. Martin, V. Caignaert, F. Damay, A. Maignan, *Chem. Mater.* **2014**, *26*, 830–836; b) R. Saha, A. Sundaresan, C. N. R. Rao, *Mater. Horiz.* **2014**, *1*, 20–31.

[14] A. T. Apostolov, I. N. Apostolova, J. M. Wesselinowa, *Eur. Phys. J. B* **2015**, *88*, 328–337.

[15] a) L. M. Daniels, M. C. Weber, M. R. Lees, M. Guennou, R. J. Kashtiban, J. Sloan, J. Kreisel, R. I. Walton, *Inorg. Chem.* **2013**, *52*, 12161–12169; b) K. Sardar, M. R. Lees, R. J. Kashtiban, J. Sloan, R. I. Walton, *Chem. Mater.* **2011**, *23*, 48–56; c) M. C. Weber, J. Kreisel, P. A. Thomas, M. Newton, K. Sardar, R. I. Walton, *Phys. Rev. B* **2012**, *85*, 054303–054312.

[16] a) J. P. Attfield, *Chem. Mater.* **1998**, *10*, 3239–3248; b) L. M. Rodriguez-Martinez, J. P. Attfield, *Phys. Rev. B* **1996**, *54*, R15622–R15625.

[17] N. Sharma, B. K. Srivastava, A. Krishnamurthy, A. K. Nigam, *Solid State Sci.* **2010**, *12*, 1464–1468.

[18] X. Sang, E. D. Grimley, C. Niu, D. L. Irving, J. M. LeBeau, *Appl. Phys. Lett.* **2015**, *106*, 061913.

[19] J. Spooren, R. I. Walton, F. Millange, *J. Mater. Chem.* **2005**, *15*, 1542–1551.

[20] a) S. V. Trukhanov, V. V. Fedotova, A. V. Trukhanov, H. Szymczak, C. E. Botez, *Tech. Phys.* **2008**, *53*, 49–54; b) S. V. Trukhanov, V. A. Khomchenko, L. S. Lobanovski, M. V. Bushinsky, D. V. Karpinsky, V. V. Fedotova, I. O. Troyanchuk, A. V. Trukhanov, S. G. Stepin, R. Szymczak, C. E. Botez, A. Adair, *J. Exp. Theor. Phys.* **2006**, *103*, 398–410; c) S. V. Trukhanov, L. S. Lobanovski, M. V. Bushinsky, V. V. Fedotova, I. O. Troyanchuk, A. V. Trukhanov, V. A. Ryzhov, H. Szymczak, R. Szymczak, M. Baran, *J. Phys. Condens. Matter* **2005**, *17*, 6495–6506.

[21] T. Nakajima, H. Kageyama, M. Ichihara, K. Ohoyama, H. Yoshizawa, Y. Ueda, *J. Solid State Chem.* **2004**, *177*, 987–999.

[22] J. S. Zhou, J. A. Alonso, V. Pomjakushin, J. B. Goodenough, Y. Ren, J. Q. Yan, J. G. Cheng, *Phys. Rev. B* **2010**, *81*, 214115.

[23] J. D. Gordon, R. M. Hornreich, S. Shtrikman, B. M. Wanklyn, *Phys. Rev. B* **1976**, *13*, 3012–3017.

[24] A. A. Coelho, *J. Appl. Crystallogr.* **2000**, *33*, 899–908.

[25] P. Cueva, R. Hovden, J. A. Mundy, H. L. Xin, D. A. Muller, *Microsc. Microanal.* **2012**, *18*, 667–675.